

Higgs couplings in SMEFT via Zh production at the HL-LHC

Subhaditya Bhattacharya,^a Abhik Sarkar,^a Sanjoy Biswas^b

^a*Department of Physics, Indian Institute of Technology Guwahati, Assam 781039, India*

^b*Department of Physics, Ramakrishna Mission Vivekananda Educational and Research Institute, Belur Math, Howrah 711202, India*

E-mail: subhab@iitg.ac.in, sarkar.abhik@iitg.ac.in,
sanjoy.phy@gm.rkmvu.ac.in

ABSTRACT: We study the Higgs couplings present in the Zh associated production mode at the Large Hadron Collider (LHC) in presence of both CP even and CP odd dimension 6 Standard Model Effective Theory (SMEFT) operators. The analysis is performed mainly in context of the HL-LHC (with $\sqrt{s} = 14$ TeV and luminosity 3000 fb^{-1}) setup using cut based as well as machine learning techniques. The analysis shows significant betterment in the signal significance by using the machine learning technique. We also do a χ^2 analysis, which reveals a significant change in the sensitivity of the coupling modifiers due to the presence of effective operators, in particular due to the four point $qqZh$ interaction. The presence of dimension six CP odd four point operators, which contributes at $\mathcal{O}(\Lambda^{-4})$ order due to lack of interference with the SM contributions, can only have sensitivity with smaller NP scale at the HL-LHC, after addressing the effective limit and constraints.

KEYWORDS: Higgs production, Higgs properties, SMEFT

Contents

1	Introduction	1
2	EFT framework	3
2.1	SMEFT operators relevant to Zh production	3
2.2	Parametrization of production cross sections	5
2.3	Comparison with other Higgs production modes	8
3	Constraints on the HZZ coupling from current data	9
3.1	Constraints on the effective coupling coefficients	10
4	Collider analysis: Current and future runs	11
4.1	Cut based analysis	11
4.2	BDT based analysis	14
4.3	Two parameter χ^2 analysis	17
5	Summary and Conclusion	18
A	Details of BDT analysis parameters	20

1 Introduction

The Higgs boson discovery at the LHC provided the first conclusive portrait of the Electroweak Symmetry Breaking (EWSB) mechanism [1] and mass generation of the SM particles. Over a decade since the Higgs discovery, we have been able to probe many of its properties, some of which are precise and closely mimic that of a SM-like isodoublet (H), some are not, allowing for New Physics (NP) studies via Higgs sector. One standard way of parametrizing the Higgs couplings beyond the SM is to use the κ framework [2], where any deviation from the SM is taken into consideration by variation of the κ parameter, where $\kappa = 1$ depicts SM. Most of the Higgs studies at the LHC uses such parametrisation and so do we. However, one needs to be vigilant about the possible sources of NP that generates such contributions and need to be consistent with null observation of NP searches while scanning the possible values that κ can acquire¹.

The couplings of our interest for this study are the $qqZ/qqZh$ and hZZ vertices which appear in both VBF as well as Zh production modes of the Higgs boson. The entire set of operators involved in the modification of the SM counterpart of Z vertices are written in equations (1.1) and (1.2). Note here in writing (1.1) and (1.2), we have adhered to the

¹We will address this issue later in a specific context.

vertices after EWSB, when $H = \begin{pmatrix} 0 \\ (v+h) \\ \sqrt{2} \end{pmatrix}$. $\kappa_Z \neq 1$ takes into account the deviation of the SM hZZ expectation.

$$\mathcal{L}_{SM} = \kappa_Z \frac{m_Z^2}{v} Z_\mu Z^\mu h + g_{uL}^{\text{SM}} Z_\mu \bar{u}_L \gamma^\mu u_L + g_{uR}^{\text{SM}} Z_\mu \bar{u}_R \gamma^\mu u_R + g_{dL}^{\text{SM}} Z_\mu \bar{d}_L \gamma^\mu d_L + g_{dR}^{\text{SM}} Z_\mu \bar{d}_R \gamma^\mu d_R; \quad (1.1)$$

$$\begin{aligned} \mathcal{L}_{NP} = & g_{ZZ} \frac{h}{v} Z^{\mu\nu} Z_{\mu\nu} + g_{Z\tilde{Z}} \frac{h}{v} Z^{\mu\nu} \widetilde{Z}_{\mu\nu} + g_{Z\gamma} \frac{h}{v} A^{\mu\nu} Z_{\mu\nu} + g_{\tilde{Z}\gamma} \frac{h}{v} A^{\mu\nu} \widetilde{Z}_{\mu\nu} \\ & + g_u^L Z_\mu \bar{u}_L \gamma^\mu u_L + g_u^R Z_\mu \bar{u}_R \gamma^\mu u_R + g_d^L Z_\mu \bar{d}_L \gamma^\mu d_L + g_d^R Z_\mu \bar{d}_R \gamma^\mu d_R \\ & + \delta_u^L \frac{h}{v} Z_\mu \bar{u}_L \gamma^\mu u_L + \delta_u^R \frac{h}{v} Z_\mu \bar{u}_R \gamma^\mu u_R + \delta_d^L \frac{h}{v} Z_\mu \bar{d}_L \gamma^\mu d_L + \delta_d^R \frac{h}{v} Z_\mu \bar{d}_R \gamma^\mu d_R \\ & + g_u \frac{1}{v} (\bar{u}_L \sigma^{\mu\nu} u_R + \bar{u}_R \sigma^{\mu\nu} u_L) Z_{\mu\nu} + g_d \frac{1}{v} (\bar{d}_L \sigma^{\mu\nu} d_R + \bar{d}_R \sigma^{\mu\nu} d_L) Z_{\mu\nu} \\ & + \delta_u \frac{h}{v^2} (\bar{u}_L \sigma^{\mu\nu} u_R + \bar{u}_R \sigma^{\mu\nu} u_L) Z_{\mu\nu} + \delta_d \frac{h}{v^2} (\bar{d}_L \sigma^{\mu\nu} d_R + \bar{d}_R \sigma^{\mu\nu} d_L) Z_{\mu\nu}. \end{aligned} \quad (1.2)$$

In the above equations, the notations have usual meaning, particularly note $Z_{\mu\nu} = \partial_\mu Z_\nu - \partial_\nu Z_\mu$, $\widetilde{Z}_{\mu\nu} = \epsilon_{\mu\nu\alpha\beta} Z^{\alpha\beta}$ where Z_μ denotes the physical Z boson, $\epsilon_{\mu\nu\alpha\beta}$ is a completely antisymmetric tensor and $\sigma^{\mu\nu} = \{\gamma^\mu, \gamma^\nu\}$. We will provide a detailed matching with the standard Warsaw basis [3] later.

Over the last two runs, LHC experiments, ATLAS [4] and CMS [5] have almost pinned down the Higgs couplings to less than 10% uncertainty, however, the High Luminosity (HL) run will prove to be significant for establishing a clearer picture of Higgs characteristics. The Higgs couplings associated with gauge bosons has been studied extensively in the existing literature from various point of views. They include bounds on the anomalous couplings [6–9], Higgs CP properties [10–14], etc. The procedure involves dedicated signal observables as well as in the effective theory (EFT) framework [15–22] in variety of production and decay channels in context of the current and future colliders.

In this analysis, we study the NP effects in hZZ and qqZ couplings as well as the fully NP induced $qqZh$ coupling in the Zh associated production mode, within the realm of the Standard Model Effective Field Theory (SMEFT) [23] at the High Luminosity (HL) LHC frontier. SMEFT framework is arguably the best motivated scenario for searching NP in a model independent way, either via deviations in the signal pattern or excess in the cross-section predicted from the SM, given the absence of a specific hint for NP in current scenarios.

Out of the different channels of Higgs production, the Higgs-strahlung or Vh ($V = W, Z$) production modes turn out to be more sensitive to the variation of effective operators concerned in the modification of the aforementioned couplings. We limit ourselves to the Zh channel, but a similar analysis is possible for the WH channel and estimation of hWW coupling, however, the SM background turns indomitable to make a reasonable prediction in such circumstances. There have been a number of analysis concerning the Zh production mode [16–18]. However, the effect of CP odd operators in context of the

$qqZ/qqZh$ couplings (dipole operators) have been neglected. We show that the presence of both CP even as well as CP odd effective operators significantly alter the existing bounds on the concerned couplings at the present and projected LHC sensitivities.

The organization of the paper is as follows: we discuss SMEFT operators relevant for our analysis and their sensitivities in section 2, constraints on the coupling modifiers as well as SMEFT coefficients from current data in section 3, detailed collider analysis in section 4 and concluding remarks in 5.

2 EFT framework

In absence of a direct observational evidence of NP signal at current experiments, one of the best possible ways to gauge the effects of NP is through higher dimensional effective operators constructed out of the SM fields respecting the SM gauge symmetry. They are popularly referred as SMEFT operators. Note here that SMEFT operators also include the Higgs field as isodoublet under the SM gauge group, while there are efforts to keep it beyond, for example, in HEFT [24], but given the Higgs properties closely mimicking that of a SM doublet, we choose SMEFT framework to explore the limit of NP². These operators are suppressed by an appropriate power of a heavy NP mass scale (Λ) integrated out, depending on the mass-scale of the operator. Understandably the effects of such operators diminish with higher mass dimension of the operators, hence we will constrict ourselves to the lowest dimension operators that contribute to the Zh associated production, which appears in dimension six; operators of dimension 8 [30, 31] may also contribute, but will be suppressed³.

2.1 SMEFT operators relevant to Zh production

The SMEFT Lagrangian can be written as:

$$\mathcal{L} = \mathcal{L}_{SM} + \sum_{i,(n>4)} \frac{c_i}{\Lambda^{(n-4)}} \mathcal{O}_i^{(n)}, \quad (2.1)$$

Here, $\mathcal{O}_i^{(n)}$ represents operators of dimension n and c_i represents dimensionless couplings or Wilson's coefficients. Throughout this analysis, the effective scale is taken as $\Lambda = 1$ TeV, while the resulting bound or the sensitivity is obtained for the corresponding Wilson coefficient c_i . However, it is simple to understand that the limit on c_i can be rescaled easily for different choices of Λ , following, $\frac{c_i}{\Lambda^2} = \frac{c'_i}{\Lambda'^2}$. Although, the validity of effective limit depends on the choice of Λ , strictly speaking the CM energy of the reaction should abide by $\sqrt{s} < \Lambda$. At hadron collider, it is difficult to ensure such a condition, we elaborate upon the possibility later.

There is no unique basis for the choice of these operators and all the different bases are equivalent. We choose Warsaw basis for our representation. The SMEFT operators

²Apart, operators with two Higgs doublets [25, 26], or a right handed neutrino [27–29] have also been done.

³It is well known that the only SMEFT operator in dimension 5 is the Weinberg operator $\bar{N}N^c$; $N = H^\dagger \epsilon \ell$, which generates Majorana neutrino mass.

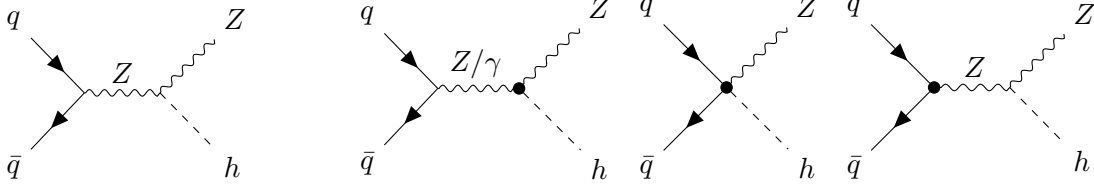


Figure 1: SM and EFT contributions to the Zh associated production mode at the LHC. Dotted vertices refer to the presence of EFT operators.

relevant to ZH associated production mode are tabulated in Table 1 and the corresponding Feynman diagrams are shown in Figure 1. The vertices with a blob represent effective operator contribution, which modifies ZZh , qqh vertices and additional contributions are obtained via γZh and $qqZh$ vertices.

Before moving forward, it should be noted that operators are classified majorly into two categories, those generated at loop level (LG operators) or potential tree generated (PTG operators) for NPs those which are weakly coupled and decoupling [32]. The LG operators are suppressed additionally by a factor of $(4\pi)^2$ coming from the loops and hence their contributions are expected to be suppressed in comparison to the PTG operators if the underlying NP scale is the same. However, this additional suppression factor for the LG operators is not intrinsically incorporated in most SMEFT studies in order to maintain uniformity of the nomenclature, we will however use the operator classification as in [3].

Operators (hZZ vertex, CP even)	Operators ($qqZ/qqZh$ vertex, CP even)
$\mathcal{O}_{H\Box} = (H^\dagger H)\Box(H^\dagger H)$	$\mathcal{O}_{Hq}^{(1)} = (H^\dagger i\overleftrightarrow{D}_\mu H)(\bar{q}_p\gamma^\mu q_r)$
$\mathcal{O}_{HDD} = (H^\dagger D_\mu H)(H^\dagger D^\mu H)$	$\mathcal{O}_{Hq}^{(3)} = (H^\dagger i\overleftrightarrow{D}_\mu^i H)(\bar{q}_p\tau^i\gamma^\mu q_r)$
$\mathcal{O}_{HW} = (H^\dagger H)W_{\mu\nu}^i W^{i\mu\nu}$	$\mathcal{O}_{Hu} = (H^\dagger i\overleftrightarrow{D}_\mu H)(\bar{u}_p\gamma^\mu u_r)$
$\mathcal{O}_{HB} = (H^\dagger H)B_{\mu\nu} B^{\mu\nu}$	$\mathcal{O}_{Hd} = (H^\dagger i\overleftrightarrow{D}_\mu H)(\bar{d}_p\gamma^\mu d_r)$
$\mathcal{O}_{HWB} = (H^\dagger \tau^i H)W_{\mu\nu}^i B^{\mu\nu}$	
Operators (hZZ vertex, CP odd)	Operators ($qqZ/qqZh$ vertex, CP odd)
$\mathcal{O}_{H\widetilde{W}} = (H^\dagger H)\widetilde{W}_{\mu\nu}^i W^{i\mu\nu}$	$\mathcal{O}_{uW} = (\bar{q}_p\sigma^{\mu\nu}u_r)\tau^i\widetilde{H}W_{\mu\nu}^i$
$\mathcal{O}_{H\widetilde{B}} = (H^\dagger H)\widetilde{B}_{\mu\nu} B^{\mu\nu}$	$\mathcal{O}_{uB} = (\bar{q}_p\sigma^{\mu\nu}u_r)\widetilde{H}B_{\mu\nu}$
$\mathcal{O}_{H\widetilde{WB}} = (H^\dagger \tau^i H)\widetilde{W}_{\mu\nu}^i B^{\mu\nu}$	$\mathcal{O}_{dW} = (\bar{q}_p\sigma^{\mu\nu}d_r)\tau^i\widetilde{H}W_{\mu\nu}^i$
	$\mathcal{O}_{dB} = (\bar{q}_p\sigma^{\mu\nu}d_r)HB_{\mu\nu}$

Table 1: Dimension 6 SMEFT operators (in Warsaw basis) relevant to VH associated production at the LHC. Here, p and r are quark family indices. For complex operators, the presence of respective hermitian conjugates is assumed. For relevance: $D_\mu = \partial_\mu + ig\frac{\tau^i}{2}W_\mu^i + ig'\frac{1}{2}B_\mu$, $W_{\mu\nu}^i = \partial_\mu W_\nu^i - \partial_\nu W_\mu^i + g\epsilon^{ijk}W_\mu^j W_\nu^k$, $B_{\mu\nu} = \partial_\mu B_\nu - \partial_\nu B_\mu$, $H^\dagger i\overleftrightarrow{D}_\mu H = iH^\dagger D_\mu H - i(D_\mu H)^\dagger H$, $H^\dagger i\overleftrightarrow{D}_\mu^i H = iH^\dagger \tau^i D_\mu H - i(D_\mu H)^\dagger \tau^i H$, $\widetilde{V}_{\mu\nu} = \epsilon_{\mu\nu\rho\sigma}V^{\rho\sigma}$ ($V = W^i, B$).

A few observations related to the operators as mentioned in Table 1:

- The operators $\mathcal{O}_{H\Box}$ and \mathcal{O}_{HDD} modify the Higgs gauge boson coupling by a mul-

tiplicative factor without introducing any new Lorentz structure, amounting to a renormalization of the Higgs field. As such the contribution can be absorbed in the coupling modifier.

- The operators \mathcal{O}_{HW} , \mathcal{O}_{HB} and \mathcal{O}_{HWB} contribute in the modification of the HVV vertex. These amounts to the CP conserving anomalous Higgs gauge boson coupling.
- The operators $\mathcal{O}_{H\widetilde{W}}$, $\mathcal{O}_{H\widetilde{B}}$ and $\mathcal{O}_{H\widetilde{W}B}$ contribute in the modification of the hZZ vertex. These amounts to the CP violating anomalous Higgs gauge boson coupling.
- The operators $\mathcal{O}_{Hq}^{(1)}$, $\mathcal{O}_{Hq}^{(3)}$, \mathcal{O}_{Hu} and \mathcal{O}_{Hd} are the CP even contributions to the four field contact interaction $qqZh$. These operators also contribute to qqZ vertex.
- The operators \mathcal{O}_{uW} , \mathcal{O}_{uB} , \mathcal{O}_{dW} and \mathcal{O}_{dB} are the CP odd contributions to the four field contact interaction $qqZh$. These operators also contribute to qqZ vertex. These operators contribute to the dipole moments of quarks and hence can be referred to as dipole operators.

A complete matching between the coefficients in Eq.1.2 and the SMEFT coefficients as in Table 1 are shown in Table 2.

Coefficient	Warsaw equivalent
g_{ZZ}	$2(c_w^2 c_{HW} + s_w^2 c_{HB} + s_w c_w c_{HWB}) v^2 / \Lambda^2$
$g_{Z\gamma}$	$(2s_w c_w^2 (c_{HW} - c_{HB}) + (s_w^2 - c_w^2) c_{HWB}) v^2 / \Lambda^2$
$g_{Z\widetilde{Z}}$	$2(c_w^2 c_{H\widetilde{W}} + s_w^2 c_{H\widetilde{B}} + s_w c_w c_{H\widetilde{W}B}) v^2 / \Lambda^2$
$g_{\widetilde{Z}\gamma}$	$(2s_w c_w^2 (c_{H\widetilde{W}} - c_{H\widetilde{B}}) + (s_w^2 - c_w^2) c_{H\widetilde{W}B}) v^2 / \Lambda^2$
g_u^L	$-\left(c_{Hq}^{(1)} + c_{Hq}^{(3)}\right) ev^2 / (2\Lambda^2 s_w c_w)$
g_d^L	$-\left(c_{Hq}^{(1)} - c_{Hq}^{(3)}\right) ev^2 / (2\Lambda^2 s_w c_w)$
g_u^R	$-c_{Hu} ev^2 / (2\Lambda^2 s_w c_w)$
g_d^R	$-c_{Hd} ev^2 / (2\Lambda^2 s_w c_w)$
δ_u^L	$-\left(c_{Hq}^{(1)} + c_{Hq}^{(3)}\right) ev^2 / (\Lambda^2 s_w c_w)$
δ_d^L	$-\left(c_{Hq}^{(1)} - c_{Hq}^{(3)}\right) ev^2 / (\Lambda^2 s_w c_w)$
δ_u^R	$-c_{Hu} ev^2 / (\Lambda^2 s_w c_w)$
δ_d^R	$-c_{Hd} ev^2 / (\Lambda^2 s_w c_w)$
g_u	$(s_w c_{uB} - c_w c_{uW}) ev^2 / \sqrt{2} \Lambda^2$
g_d	$(s_w c_{dB} + c_w c_{dW}) ev^2 / \sqrt{2} \Lambda^2$
δ_u	$\sqrt{2} (s_w c_{uB} - c_w c_{uW}) ev^2 / \Lambda^2$
δ_d	$\sqrt{2} (s_w c_{dB} + c_w c_{dW}) ev^2 / \Lambda^2$

Table 2: Matching between coefficients in equation (1.2) and the SMEFT coefficients. s_w and c_w are the sine and cosine of the Weinberg angle.

2.2 Parametrization of production cross sections

When SMEFT effects are included, the cross section consists of three types of terms viz. the pure SM contribution, the SM plus EFT interference ($\propto \Lambda^{-2}$ from dimension six operators)

and the pure EFT contribution ($\propto \Lambda^{-4}$). Inclusion of dimension 8 operators would result in SM plus EFT interference contribution $\propto \Lambda^{-4}$ which is comparable to the pure EFT contribution from dimension 6 terms, however, we do not consider them in this analysis. The production cross section in presence of SMEFT operators takes the form:

$$\sigma = \sigma^{(SM)} + \sum_{i=1}^{n_L} c_i \sigma_i^{(L)} + \sum_{i<j}^{n_Q} c_i c_j \sigma_{ij}^{(Q)}, \quad (2.2)$$

where, n_L and n_Q refers to the number of linear and quadratic SMEFT contributions. The effective scales Λ^{-2} and Λ^{-4} are absorbed in the cross sections $\sigma_i^{(L)}$ and $\sigma_{ij}^{(Q)}$ respectively. In presence of coupling modifiers κ , the cross section in equation (2.2) takes the form as below,

$$\sigma = \kappa^2 \sigma^{(SM)} + \sum_{i=1}^{n_L} (\alpha_i^{(L)} \kappa + \beta_i^{(L)} \kappa^2) c_i \sigma_i^{(L)} + \sum_{i<j}^{n_Q} (1 + \alpha_{ij}^{(Q)} \kappa + \beta_{ij}^{(Q)} \kappa^2) c_i c_j \sigma_{ij}^{(Q)}. \quad (2.3)$$

At the hadron collider, an analytical form of the cross section is difficult to write due to the uncertainty of the incoming momenta of the partons. However, we can numerically fit the cross section as a function of the parameters and this turns out to be equally useful for gauging the effects of NP. In the following, we fit the operator coefficients following (2.3) at 14 TeV LHC for the Zh associated production processes are performed considering one operator at a time. The variation of the total production cross section are shown in Figure 2 (for CP even operators) and 3 (for CP odd operators). The ratio of the total production cross section for moving from 13 TeV to 14 TeV are also shown. We adopt the following methodology, the effective Lagrangian is implemented in `FeynRules` [33] to generate the `UFO` model [34] file. This model file is then fed into the event generator `MG5_aMC` [35] to obtain the above cross sections at the leading order (LO). The NP scale is chosen as $\Lambda = 1$ TeV. A few key points observed are as follows:

- The CP even operators associated with the $qqZ/qqZh$ vertices have significant quadratic contributions indicating large pure EFT contribution. The enhancement of the EFT terms result from the absence of propagator suppression in the production process.
- The CP odd operators concerning $qqZ/qqZh$ vertices have weak linear contribution. This is because they bind fermions with different chiralities and hence do not interfere with the SM process. Due to the negligible linear dependence, they cause variation in the cross section only in the positive direction.
- All the operators except $\mathcal{O}_{Hq}^{(3)}$ shows near symmetric behaviour along the positive and negative side. The operator $\mathcal{O}_{Hq}^{(3)}$ dips around $c_{Hq}^{(3)} = -0.2$ and then continues to rise as we go further in the negative direction. This is due to strong linear as well as quadratic dependence and the trade off between them happens away from $c_{Hq}^{(3)} = 0$ towards the negative axis.

- When moving from 13 TeV to 14 TeV LHC, the contact operators i.e. operators associated with $qqZ/qqZh$ vertices, significantly boost the production cross sections. The other operators are less sensitive.

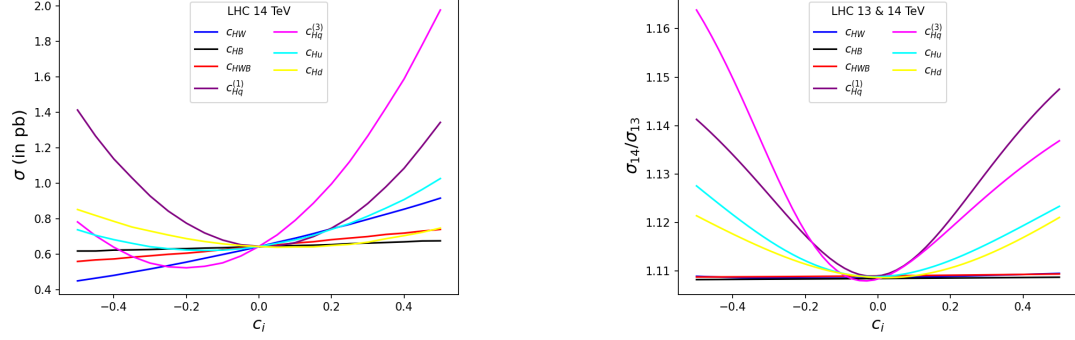


Figure 2: Left: Variation of Zh associated production cross section with variation in CP even effective operator coefficients at the 14 TeV LHC. Right: Variation in the ratio of production cross section of the 14 TeV LHC to the 13 TeV LHC with variation in the effective operator coefficients. See figure inset for the colour codes.

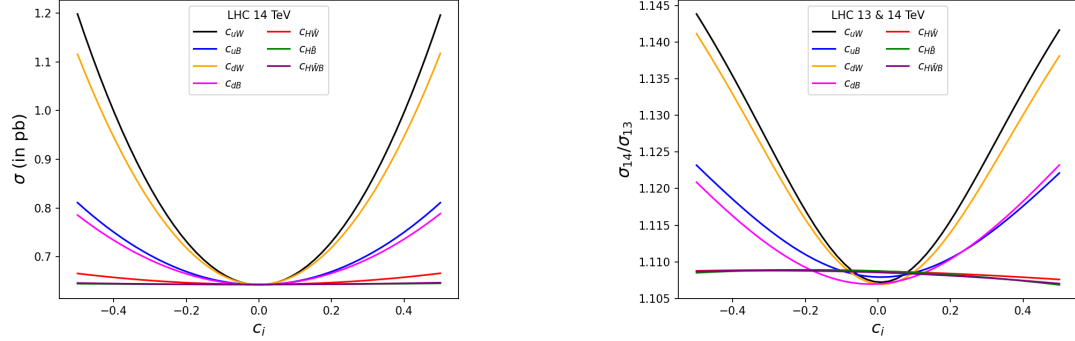


Figure 3: Left: Variation of Zh associated production cross section with change in CP odd effective operator coefficients at the 14 TeV (Left) LHC. Right: Variation in the ratio of production cross section of the 14 TeV LHC to the 13 TeV LHC with change in effective operator coefficients. See figure inset for the colour codes.

It is observed that the most significant change to the cross section is obtained from $\mathcal{O}_{Hq}^{(3)}$ among the CP even operators and \mathcal{O}_{uW} among the CP odd operators. We will consider these two operators for our study. Along with the coupling modifier κ_Z , this form our EFT parameter space: $\{\kappa_Z, c_{uW}, c_{Hq}^{(3)}\}$. The parametrized coefficients for Zh production with these operators following Eqn. (2.3) are tabulated in Table 3. Coefficients of linear terms in 1, κ_Z , c_{uW} and $c_{Hq}^{(3)}$ are not present in our parametrization. Further, the coefficients of $k_Z c_{uW}$, $k_Z^2 c_{uW}$, $c_{uW} c_{Hq}^{(3)}$, $k_Z c_{uW} c_{Hq}^{(3)}$ and $k_Z^2 c_{uW} c_{Hq}^{(3)}$ vanish because of no interference between the SM and $\mathcal{O}_{Hq}^{(3)}$ operators with diagrams with \mathcal{O}_{uW} operator.

We shall also note that the variation of the cross-section presented here with EFT operator coefficients, have been done without considering the constraints on these operators. We shall do it in the next section. We get the dominant physics contribution to the process under consideration and the resultant parametrisation, which remains intact with the modified range of the operator coefficients that will be used for scanning the parameter space.

Coefficients	1×1	$1 \times c_{uW}$	$1 \times c_{Hq}^{(3)}$	$c_{uW} \times c_{uW}$	$c_{Hq}^{(3)} \times c_{Hq}^{(3)}$	$c_{uW} \times c_{Hq}^{(3)}$
1×1	-	-	-	1.9456	2.7265	-
$1 \times \kappa_Z$	-	-	1.0963	0.1353	0.2493	-
$\kappa_Z \times \kappa_Z$	0.6426	-	0.0925	0.1285	-0.0303	-

Table 3: The parametrized coefficients for operators $\mathcal{O}_{Hq}^{(3)}$, \mathcal{O}_{uW} and κ_Z contributing to Zh production at 14 TeV LHC, following equation (2.3).

2.3 Comparison with other Higgs production modes

The operators \mathcal{O}_{uW} and $\mathcal{O}_{Hq}^{(3)}$ are not unique to the Vh ($V = W, Z$) associated production mode. It appears in the vector boson fusion (VBF) and single top production in association with Higgs (thj) as well. The thj process has a comparatively smaller cross section and it is not ideal for the study of these operators, but the VBF mode has a larger cross section compared to VH associated production mode, as considered here. These operators are also associated with the diboson production ($VV = WW, WZ, ZZ$) processes. However, it is the sensitivity of the effective operators where VH associated production mode is superior in comparison to the VBF mode as well as VV processes. This has been illustrated in Figure 4 for the operators $\mathcal{O}_{Hq}^{(3)}$ and \mathcal{O}_{uW} . For the study of $qqZ/qqZh$ vertices, Zh production fares over ZBF, ZZ or WZ modes.

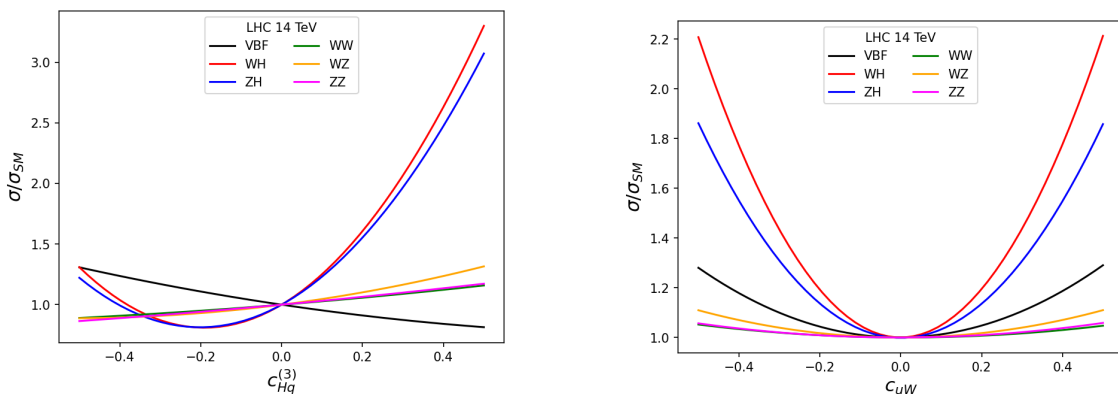


Figure 4: Variation in the ratio of production cross section to the SM cross section in VBF, VH and VV processes at the 14 TeV LHC with variation in effective coefficients: $c_{Hq}^{(3)}$ (Left) and c_{uW} (Right).

3 Constraints on the HZZ coupling from current data

The κ framework is the most preferred way to incorporate uncertainties in the measurement of Higgs couplings. This has been adopted in most of the experimental results reported so far, and we will also follow the same here. The current uncorrelated bounds from ATLAS ($139 fb^{-1}$) and CMS ($138 fb^{-1}$) are based on Run II data and involves global fit over the main five production and decay channels. Since we intend to study Zh associated production with H subsequently decaying to bottom pair, the bottom Higgs coupling modifier, κ_B is also important for this analysis. Higgs decay to bottom pair has been studied intensely at the LHC across several channels and the bounds are given in terms of signal strength (μ), i.e. the ratio of the observed signal to the SM predicted value. In Table 5 we list out the uncorrelated bounds on the coupling modifiers as well as the signal strengths of the Higgs decay to bottom pair in the Zh production channel.

Measurable	Bound	Source
κ_Z	[0.97, 1.11]	CMS ($pp \rightarrow h$) [5]
	[0.94, 1.05]	ATLAS ($pp \rightarrow h$) [4]
κ_B	[0.85, 1.11]	CMS ($pp \rightarrow h$) [5]
	[0.79, 1.01]	ATLAS ($pp \rightarrow h$) [4]
μ_{Hbb}^{Zh}	[0.59, 1.17]	CMS ($pp \rightarrow Zh, h \rightarrow bb$) [36]
	[0.85, 1.33]	ATLAS ($pp \rightarrow Zh, h \rightarrow bb$) [37]

Table 4: Constraints on κ_Z , κ_B and μ_{Hbb}^{Zh} (at 95% C.L.) from ATLAS and CMS experiments.

Considering the bounds on the signal strength, we can limit the coupling modifiers using the measured signal strengths as shown in Eqn. 3.1.

$$\mu_{hbb}^{Zh} = \frac{(\sigma^{Zh} \times (B.R.)^{hbb})}{(\sigma^{Zh} \times (B.R.)^{hbb})_{SM}} = \frac{\kappa_Z^2 \kappa_B^2}{0.1775 + 0.5809 \kappa_B^2 + (0.2152 + 0.0264) \kappa_Z^2}. \quad (3.1)$$

In evaluating Eqn. 3.1, both the Higgs couplings with the bottom quark as well as with Z bosons have been modified keeping coupling with other fermions unchanged. κ_Z appears from the production cross-section, while κ_B appears from the decay branching fraction, pertaining to the fact that Higgs production and decay modes are those predicted in the SM, the NP effects only enters via rescaling of the Higgs coupling strength. The denominator comes from the modification of the Higgs decay width, which is easily adjusted within the observed total Higgs decay width at LHC for moderate values of κ parameters. We can see that for $\kappa_Z = \kappa_B = 1$, the signal strength turns one. We further invoke the custodial symmetry requirement $\kappa_W = \kappa_Z$. The bounded region is shown in Figure 5. Additionally, superimposing the current correlated bound on the $\kappa_V - \kappa_F$ space from the combined Higgs measurement gives the status of the most accurate constraint from the current data. The uncertainties are less than 10% from the SM prediction.

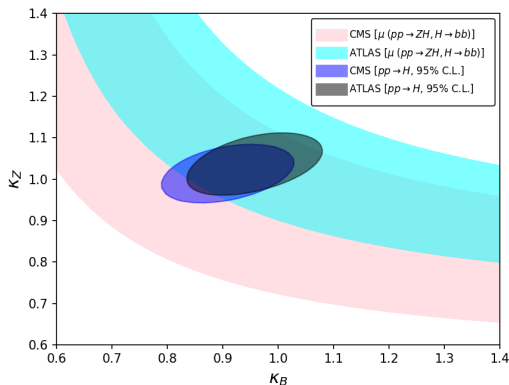


Figure 5: Constraints on coupling modifiers κ_Z and κ_B based on combined limit on $pp \rightarrow Zh$, $h \rightarrow b\bar{b}$ production signal strength (bands) [36, 37] as well as the combined experimental best fit for all Higgs production and decay processes (ellipses) [4, 5] at ATLAS and CMS experiments.

3.1 Constraints on the effective coupling coefficients

In context of the study of Higgs couplings in effective framework, the SMEFiT collaboration [38] has attempted to provide global bounds based on Higgs, Top and Diboson data from Tevatron, LHC and LEP. Similar fits have been done including B-Physics data with LHC top and bottom quark studies [39, 40]. Similarly, global fits have also been performed based on Electroweak Precision data as well as Δ_{CKM} measurement [41]. Customarily, both ATLAS and CMS have done a number of studies on constraining the EFT operators across various channels using latest data. While ATLAS uses SMEFT, CMS uses HEL parametrization, we will consider bounds from ATLAS [37, 42, 43] only. Also, there has been numerous studies concerning SMEFT, projecting constraints for future collider experiments. We tabulate the constraints on the coefficients c_{uW} and $c_{Hq}^{(3)}$ from current data in Table 5.

Coefficient	Bound	Combined	C.L.	Source
c_{uW}	$[-0.375, 0.375]$	$[-0.01, 0.05]$	95%	[44]
	$[-0.01, 0.05]$		90%	[40]
$c_{Hq}^{(3)}$	$[-0.432, 0.062]$	$[-0.02, 0.04]$	95%	[38]
	$[-0.7024, 0.1036]$		68%	[41]
	$[-0.08, 0.1]$		95%	[43]
	$[-0.23, -0.19] \cup [-0.04, 0.04]$		95%	[37]
	$[-0.15, 0.52]$		95%	[42]
	$[-0.02, 0.05]$	90%	[40]	

Table 5: Constraints on the effective operator coefficients c_{uW} and $c_{Hq}^{(3)}$ from existing studies, see the references for details.

A few comments and clarifications on the existing bounds:

- The bound on c_{uW} from the EFT analysis [44] based on existing LHC Drell-Yan process provides a constraint of $[-6.0, 6.0]$ at $\Lambda = 4$ TeV. Scaling Λ down to 1 TeV, the bound stands at $[-0.375, 0.375]$.
- The bounds on the operator coefficients in [40] are provided for the coefficients $\tilde{C}_i = c_i \left(\frac{v^2}{\Lambda^2} \right)$. Correspondingly, the bounds on c_{uW} and $c_{Hq}^{(3)}$ in Table 5 are obtained for $v = 246$ GeV and $\Lambda = 1$ TeV.
- The CP-violating gauge-Higgs operators listed in Table 1 are constrained by the fermion dipole moment observables, such as electron and neutron dipole moments, as they contribute at one loop to dipole operators. The current limits on the electron and neutron dipole moments are 1.1×10^{-29} and 3.0×10^{-26} (in units of e cm), respectively [45]. These operators are also constrained by the measurements of the triple gauge-interactions of the form $WW\gamma$ and WWZ at LEP and the CP asymmetry measured in the $B \rightarrow X_s \gamma$ decay. The CP asymmetry measured in $B \rightarrow X_s \gamma$ decay is $A_{B \rightarrow X_s \gamma} = 0.015(20)$.

4 Collider analysis: Current and future runs

In this section, we will discuss the event generation and analysis in the context of the current and future HL LHC data. We have simulated $pp \rightarrow Zh \rightarrow (\ell\ell)(\bar{b}b)$ process at the LHC 13 TeV and 14 TeV center of mass energies. The PDF set used is NN23L01 [46] and the renormalization and factorization scales are set at the default dynamical scale choice of MadGraph. The signal and background informations will be detailed in Section 4.1. Before proceeding for a collider analysis in presence of the EFT operators, it is important to check validity of the effective approximation for the collider setup. The validity condition is $\sqrt{\hat{s}} < \Lambda$, where $\sqrt{\hat{s}}$ is the partonic centre of mass energy. However, ensuring this criteria is difficult in hadron colliders like LHC, where collisions between partons happen at variable centre of mass energies. One way to deal with this is to construct the invariant mass of the final state particles, $M_{Zh}^2 = (p_Z + p_h)^2$ here ($p_{h,Z}$ represent reconstructed four momenta), to guess the energy scale at which the partonic collisions take place. This is depicted in Figure 6, for the production process at a particular EFT benchmark point and we observe that almost all the events obey the effective validation criteria, when $\Lambda = 1$ TeV. Now, the generated signal and background events are fed in Pythia8 [47] for parton showering. The showered events are fed in Fastjet3 [48] for jet clustering using the anti k_t algorithm [49] with jet radius 0.5 and jet $p_T \geq 20$ GeV. Finally, the events are processed through Delphes3 to take into account finite detector resolution effects, as well as particle identification, reconstruction and jet tagging. The b-tagging efficiency is around 0.6 and the light-jet mistagging efficiency is considered to be one in 100. The processed events are analyzed using MadAnalysis5 [50].

4.1 Cut based analysis

We consider the signal to be $pp \rightarrow Z(l^+l^-)H(\bar{b}b)$ i.e. a dilepton di-bjet signal. This signal is comparatively clean due to the presence of charged leptons with invariant mass

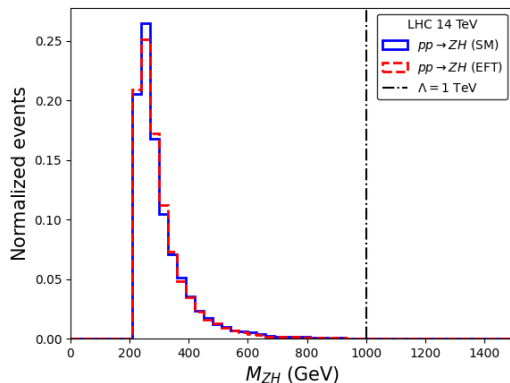


Figure 6: Invariant mass of Zh for the parton level processes in absence as well as presence of EFT operators at $\Lambda = 1$ TeV.. Here we consider the EFT benchmark point corresponding to $\kappa_Z = 1.0$, $c_{uW} = 0.05$ and $c_{Hq}^{(3)} = 0.04$.

of the dilepton system peaking around Z -mass. The possible SM backgrounds for this signal process are $pp \rightarrow t\bar{t}$, $pp \rightarrow ZZ$, $gg \rightarrow Zh$ and $pp \rightarrow Zb\bar{b}$. NLO corrections to both signal and background processes are taken into account by multiplying the production cross sections for each process by its NLO K factor, where $K = \sigma_{NLO}/\sigma_{LO}$. The LO and NLO cross sections are calculated using `MG5_aMC@NLO` at LHC 13 TeV and the K factors for different processes are: Zh : 1.288 (for $pp \rightarrow Zh$), 2.000 (for $gg \rightarrow Zh$), $Zb\bar{b}$: 1.230, $t\bar{t}$: 1.338 and ZZ : 1.461 [51–53].

We perform the analysis for two different setups viz. LHC 13 TeV $139 fb^{-1}$ (equivalent to Run II) and LHC 14 TeV $3000 fb^{-1}$ (future HL-LHC projection). We introduce some basic cuts common for all the analysis. These can be detailed as: $P_T^j > 20.0$ GeV, $P_T^l > 10.0$ GeV, $-5.0 < \eta_j < 5.0$, $-2.5 < \eta_l < 2.5$, $\Delta R_{jj} > 0.4$, $\Delta R_{lj} > 0.4$, $\Delta R_{ll} > 0.4$, where, subscripts j and l refer to jets and leptons respectively, and the kinematic variables have their usual definitions as in collider literature [54]. Apart from these, to ensure exclusive $l^+l^-b\bar{b}$ signal we select events with $N_b = 2$ and $N_l = 2$. The relevant distributions of kinematic variables and observables are plotted in Figure 7 for 13 TeV and 14 TeV LHC. Choosing $N_j < 5$ for Zh considerably reduces the pure hadronic backgrounds at LHC. We further choose a wide M_{bb} cut around the Higgs mass to make sure that we retain most of the signal while eliminating the backgrounds. The presence of dileptons enables us to use some additional cuts. Owing to the better detectability of leptons, a narrow cut on M_{ll} around the Z mass significantly reduces the $t\bar{t}$ background. Finally due to the absence of invisible particles in the final state (a part from neutrinos possibly coming b -decay) rejecting events with large MET (MET > 30 GeV) removes backgrounds with neutrinos in final state like leptonic $t\bar{t}$ mode. The entire cut flow for SM Zh process (in absence of EFT contributions) is tabulated in Table 6.

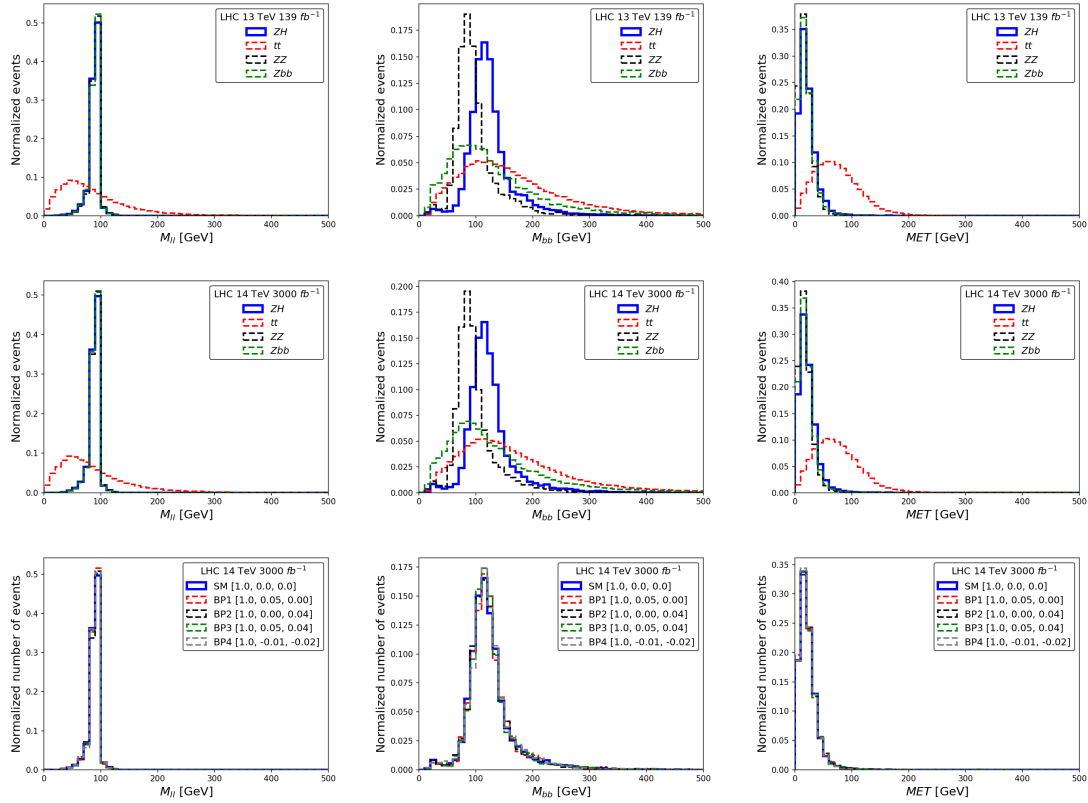


Figure 7: Invariant mass of dilepton (Left), invariant mass of di-bjet (Center) and missing transverse energy (Right) corresponding to the SM signal and background processes in $Z(l^+l^-)h(b\bar{b})$ associated production at the LHC for $\sqrt{s} = 13$ TeV, luminosity of 139 fb^{-1} (Top layer), $\sqrt{s} = 14$ TeV, luminosity of 3000 fb^{-1} (Middle layer) analysis. The Bottom layer consists of the same distributions at different EFT benchmark points shown in Table 7 at $\sqrt{s} = 14$ TeV, luminosity of 3000 fb^{-1} .

Cuts	LHC 13 TeV 139 fb^{-1}				LHC 14 TeV 3000 fb^{-1}			
	S	B	S/B	z	S	B	S/B	z
Basic Cuts	569	1016890	0.0006	0.56	13327	25581580	0.0005	2.63
$N_j < 5$	309	369549	0.0008	0.51	7054	9079825	0.0008	2.34
$110.0 \text{ GeV} < M_{bb} < 140.0 \text{ GeV}$	126	56059	0.0022	0.53	2858	1382411	0.0021	2.43
$80.0 \text{ GeV} < M_{ll} < 100.0 \text{ GeV}$	107	11674	0.0092	0.99	2456	285269	0.0086	4.59
$\text{MET} < 30 \text{ GeV}$	91	5472	0.0166	1.23	2026	129095	0.0156	5.62

Table 6: Cut flow and signal significance (z) for the SM $Z(l^+l^-)h(b\bar{b})$ associated production signal with the SM background processes at LHC with $\sqrt{s} = 13$ TeV and luminosity of 139 fb^{-1} and at LHC with $\sqrt{s} = 14$ TeV and integrated luminosity of 3000 fb^{-1} . Apart, we use the following notations, S: Signal events, B: Background events, S/B: Signal to background ratio.

BPs $(\kappa_Z, c_{uW}, c_{Hq}^{(3)})$	S	B	S/B	z	ϵ_s	ϵ_b
SM (1.0, 0.0, 0.0)	2026		0.0156	5.62	2.09×10^{-2}	
BP1 (1.0, 0.05, 0.0)	2142		0.0166	5.94	2.19×10^{-2}	
BP2 (1.0, 0.00, 0.04)	2203	129095	0.0171	6.11	2.10×10^{-2}	8.72×10^{-4}
BP3 (1.0, 0.05, 0.04)	2290		0.0177	6.35	2.17×10^{-2}	
BP4 (1.0, -0.01, -0.02)	1954		0.0151	5.42	2.09×10^{-2}	

Table 7: Signal significance of the $Z(l^+l^-)h(b\bar{b})$ production process (at LHC with $\sqrt{s}=14$ TeV and luminosity $3000 fb^{-1}$) from cut based analysis at different benchmark points (BPs) in presence of effective operators, along with signal (ϵ_s) and background (ϵ_b) efficiencies.

For signal significance, we use the Asimov definition [55]:

$$z = \sqrt{2 \left((S+B) \ln \left(1 + \frac{S}{B} \right) - S \right)}, \quad (4.1)$$

where S is the number of signal events and B is the number of background events. The Asimov definition turns out to be better representative of the significance of a signal. On Taylor expansion in the limit $S \ll B$, the Asimov significance approximates to S/\sqrt{B} , which is the more common definition. However, when the signal and background numbers are comparable, it is sensible to use the Asimov definition. The number of signal and background events can further be parametrized in terms of the coupling modifiers and the effective operator coefficients as shown in Eqn. 4.2 .

$$\begin{aligned} S &= \mathcal{L} \times \sigma_{SM+EFT}^S(\kappa_V, c_i) \times BR^S(\kappa_B) \times \epsilon_S, \\ B &= \mathcal{L} \times \sigma_{SM}^B \times BR^B \times \epsilon_B; \end{aligned} \quad (4.2)$$

where, \mathcal{L} is the integrated luminosity, ϵ_S and ϵ_B are the signal and background cut efficiencies respectively. From Table 6, it is clear that the signal significance improves significantly as we move to the high luminosity frontier.

The second part of the analysis features inclusion of EFT operators. In presence of EFT operators, there is further boost in the signal significance. This has been illustrated in Table 7 in presence of SMEFT operators at some benchmark values. The relevant kinematic variables and observables for the different benchmark points are shown in Figure 7. The variation from the SM signal are minuscule. The benchmarks are chosen at the limiting values of the bounds discussed in section 3.

4.2 BDT based analysis

With the advent of modern machine learning tools, multivariate analysis has become a norm in collider analysis [56, 57]. Among the machine learning techniques, boosted decisions trees (BDT) based algorithms are extremely popular due to their stability as well as accuracy even for smaller datasets. With an aim to improved the signal background separation with more accuracy, we perform an analysis using the XGBoost classifier [58]. The core setup of the analysis is kept similar to the cut based counterpart. Since, we observed

higher significance at 14 TeV, 3000 fb^{-1} LHC, we will perform the BDT based analysis exclusively for the HL-LHC run. The training sets for signal ($pp \rightarrow Z(l^+l^-)H(b\bar{b})$) and backgrounds ($pp \rightarrow t\bar{t}$, $pp \rightarrow ZZ$, $gg \rightarrow Zh$ and $pp \rightarrow Zb\bar{b}$) are prepared and weighted according to its number strength at 3000 fb^{-1} . This weighted data is subjected to the same basic cuts as used in the cut based analysis. The feature selection is done in similar line with the VH, $H \rightarrow b\bar{b}$ analysis at ATLAS [37]. The features are detailed below:

- Transverse momentum of the leading lepton: p_T^l
- Transverse momentum of the leading b-jet: p_T^b
- Number of jets (inclusive of b-jets): N_j
- Missing transverse energy: MET
- Transverse momentum of the dilepton system: p_T^{ll}
- Transverse momentum of the di-b-jet system: p_T^{bb}
- Invariant mass of the dilepton system: M_{ll}
- Invariant mass of the di-b-jet system: M_{bb}
- Separation in (η, ϕ) space between the leptons: ΔR^{ll}
- Separation in (η, ϕ) space between the b-jets: ΔR^{bb}
- Difference in η between the dilepton and di-b-jet system: $\Delta\eta^{ll,bb}$
- Difference in ϕ between the dilepton and di-b-jet system: $\Delta\phi^{ll,bb}$

The detailed correlation heatmap between the features is shown in Appendix A. To prevent features with large magnitudes (like p_T , MET, etc) to dominate over small valued features (like $\Delta\eta$, ΔR , etc), all the features are scaled about their mean value by their standard deviation. This ensures all features are more or less at equal footing at the beginning of the training process. The signal and background events are divided in 1:1 ratio for training and testing each process. For training, the overall signal weight is equated with the overall background weight ensuring equal number of signal and background events entering the training process. The BDT model is constructed using `XGClassifier` and the hyperparameter tuning is done using `GridSearchCV` [59]. The details of the optimal hyperparameters is listed in Table 9 in Appendix A. The model is 3 fold cross validated using `StratifiedKFold` [59]. Since, the distributions for the SM plus EFT benchmarks vary very little from the SM distributions, we train only the SM signal and backgrounds and test on the SM as well as on SM plus EFT benchmarks.

The highlights of the BDT analysis are shown in Figure 8. As a metric for evaluation of our model, we use the ROC AUC. The AUC value for the training set is 0.9827. For the test sets, the AUC obtained are 0.9715, 0.9714, 0.9716, 0.9733 and 0.9719 respectively for SM, BP1, BP2, BP3 and BP4. This indicate that there was very little overfitting and the BPs

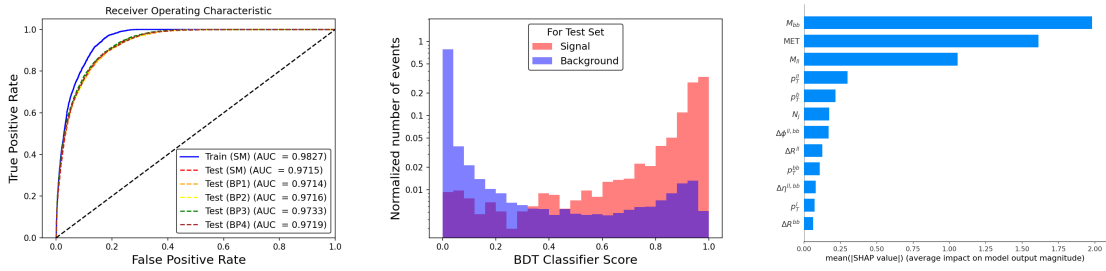


Figure 8: The Receiver Operating Characteristic (ROC) curve for the training and testing (SM as well as BPs) data. (Left) The distribution of the BDT classifier score for the SM signal and backgrounds. (Center) The mean absolute SHAP values for the features used for training the BDT model. (Right)

fared very well on the model trained with SM inputs. To enhance the signal significance, we’ve set the threshold classifier score at 0.95. This means we’ll only keep events with a BDT classifier score greater than or equal to 0.95. By doing this, we maintain a roughly similar background efficiency as in the cut-based analysis, making it easier to compare signal efficiencies between the two methods. The feature importance of a machine learning model can be realized using SHAP (SHapley Additive exPlanations) [60] values for the features. SHAP values show how each feature affects each final prediction, the significance of each feature compared to others, and the model’s reliance on the interaction between features. The SHAP values for the model are plotted in Figure 8 using `shap` module. It is distinctly observed that M_{bb} turns out to be the best discriminating feature. MET, M_{ll} and p_T^{ll} turns out to be the other important features which was also taken into account in the cut based analysis. Corresponding to the threshold value of 0.95, the significance and cut efficiencies of the signal and background processes for the BDT analysis are detailed in Table 8. It is observed that for similar background numbers, there is a significant boost in the signal numbers for both SM and other EFT benchmark points, compared to the cut based analysis.

BPs ($\kappa_Z, c_{uW}, c_{Hq}^{(3)}$)	S	B	S/B	z	ϵ_s	ϵ_b
SM (1.0, 0.0, 0.0)	3822		0.0278	10.26	3.94×10^{-2}	
BP1 (1.0, 0.05, 0.00)	4066		0.0296	10.91	4.16×10^{-2}	
BP2 (1.0, 0.00, 0.04)	4523	137574	0.0329	12.19	4.63×10^{-2}	9.29×10^{-4}
BP3 (1.0, 0.05, 0.04)	4620		0.0336	12.39	4.38×10^{-2}	
BP4 (1.0, -0.01, -0.02)	3702		0.0269	9.94	3.96×10^{-2}	

Table 8: Signal significance of the $Z(l^+l^-)h(b\bar{b})$ production process (at LHC 14 TeV 3000 fb^{-1}) from BDT based analysis (with threshold: 0.95) at different benchmark points (BPs) in presence of effective operators, along with signal (ϵ_s) and background (ϵ_b) efficiencies.

4.3 Two parameter χ^2 analysis

The χ^2 test [2] serves as a statistical measure to evaluate the degree of conformity between empirical observations and theoretical expectations within the framework of a contingency table. In statistical literature, there exist a number of definitions for the χ^2 function. These definitions are more or less equivalent and can be used interchangeably. For our case, we shall use Pearson's definition where the χ^2 is defined as follows:

$$\chi^2 = \sum_j^{bins} \left(\frac{(S^j(\kappa_i, c_i) + B_{SM}^j) - (S_{SM}^j + B_{SM}^j)}{\Delta N^j(\kappa_i, c_i)} \right)^2 = \sum_j^{bins} \left(\frac{\Delta S^j(\kappa_i, c_i)}{\Delta N^j(\kappa_i, c_i)} \right)^2. \quad (4.3)$$

For our analysis, we define $\Delta S^j(\kappa_i, c_i) = S^j(\kappa_i, c_i) - S_{SM}^j$, where $S^j(\kappa_i, c_i)$ corresponds to signal events in the j^{th} bin of a kinematic distribution, in presence of effective operators and coupling modifiers and S_{SM}^j corresponds to signal events in the same bin under the SM process. $\Delta N^j(\kappa_i, c_i)$ is the statistical uncertainty in the number of events for that bin. Now, assuming a Poisson distributed counting experiment, $\Delta N^j(\kappa_i, c_i) = \sqrt{S^j(\kappa_i, c_i) + B_{SM}^j}$, where B_{SM}^j corresponds to the background events in the j^{th} bin. The detailed parametrizations of signal and background numbers are shown in Eqn. 4.4.

$$\begin{aligned} S(\kappa_i, c_i) &= \mathcal{L} \times \sigma_{SM+EFT}^S(\kappa_Z, c_i) \times BR^S(\kappa_B) \times \epsilon_S, \\ S_{SM} &= \mathcal{L} \times \sigma_{SM}^S \times BR^S \times \epsilon_S, \\ B_{SM} &= \mathcal{L} \times \sigma_{SM}^B \times BR^B \times \epsilon_B. \end{aligned} \quad (4.4)$$

Considering the better performance of the BDT analysis over the cut based analysis, we use the signal and background efficiencies based on the BDT analysis. The χ^2 analysis is performed corresponding to the binned p_T distribution of the leading lepton. The dataset post the threshold cut is divided into 10 bins from 0-250 GeV in intervals of 25 GeV. The events with $p_T^l > 250$ GeV is dumped into an excess bin. The number of events for signal and background in each bin is tabulated in Table 10. For a Poisson distributed binned data, the number of degrees of freedom is given by $D = N - M$, where N is the number of bins and M is the number of fitted parameters. In this case, $D = 11 - 2 = 9$. Usually the constraints on the parameter space of physical parameters are reported in terms of confidence levels (C.L.). The confidence levels can be interpreted from the χ^2 values. The 68% C.L. for $D = 9$ corresponds to $\chi^2 \approx 10.388$. The χ^2 for different parameter benchmarks in $\kappa_Z - \kappa_B$ plane are shown in Figure 9.

Fig. 9 shows that the 68% C.L. bounds are very sensitive to the parameter $c_{Hq}^{(3)}$ corresponding to the CP even contact interaction. This is because $\frac{\sigma}{\sigma_{SM}}$ changes significantly under the variation of $c_{Hq}^{(3)}$ in the Vh channel (see Fig. 4 left). However, despite the fact that the variation of $\frac{\sigma}{\sigma_{SM}}$ as function of c_{uW} is quite prominent (as can be seen from Fig. 4 right) the same is not reflected in the χ^2 plots. This is mostly due to the fact that the CP-odd operators contribute at $\frac{1}{\Lambda^2}$ order and the variation of (c_{uW}) considered over a range (-0.01, 0.05) which is very narrow to produce any significant impact at that order.

The 68% C.L. bounds on the EFT couplings are shown in Fig. 10, which shows similar

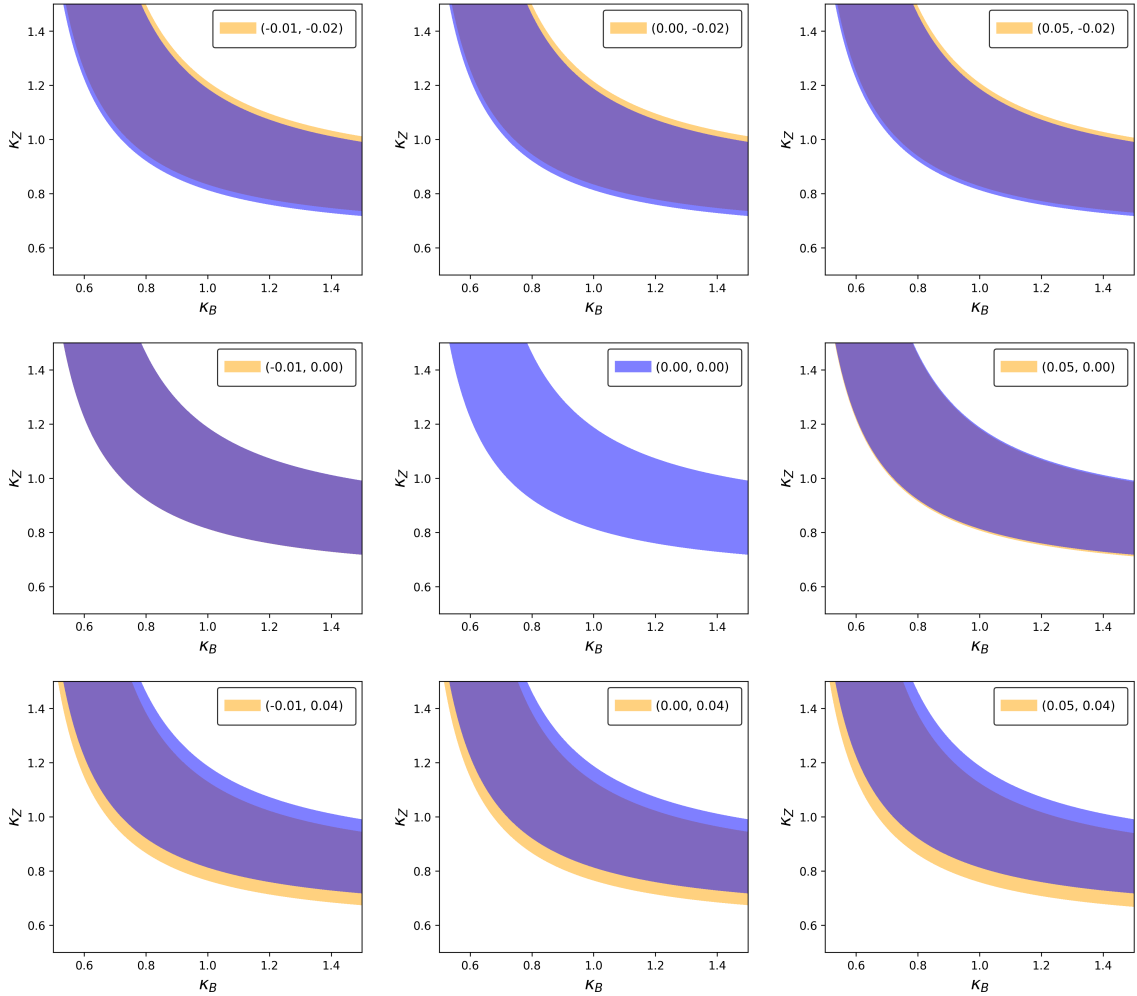


Figure 9: χ^2 plots showing 68% C.L. bounds in the $\kappa_Z - \kappa_B$ space at LHC 14 TeV 3000 fb^{-1} for different values of effective coefficients. The values in the legends refer to effective coefficient $(c_{uW}, c_{Hq}^{(3)})$.

sensitivities of the EFT operators and modifiers as in Fig. 9.

5 Summary and Conclusion

We have presented an analysis of Zh associated production at LHC in presence of dimension six SMEFT operators and coupling modifiers. We choose a simple parametrisation to match the coupling modifiers that stem from dimension six SMEFT operators in Warsaw basis. We analysed the signal and background contributions at various benchmark points, which allows maximum cross-section within the allowed values of the EFT parameters and coupling modifiers. We do both cut-based and BDT analysis using kinematic variables relevant for the process. NP scale is safely chosen at $\Lambda = 1$ TeV, which abides by effective limit having the invariant mass distribution peaks below it.

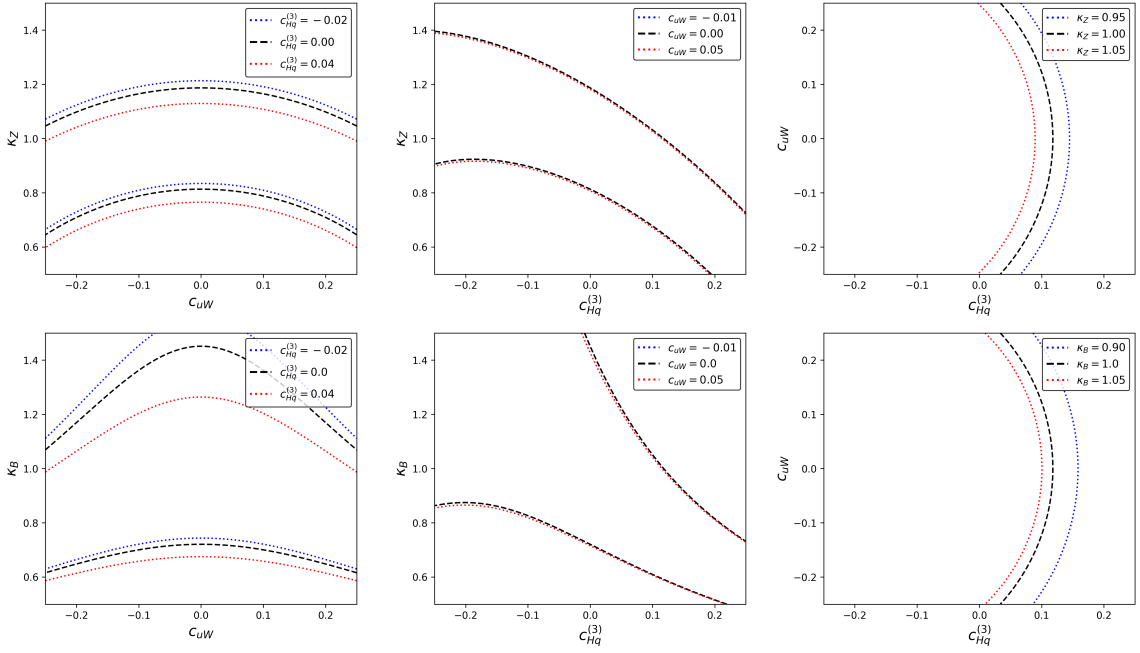


Figure 10: 68% C.L. bounds on effective coefficients at the 14 TeV 3000 fb^{-1} LHC. $\kappa_B = 1.0$ for the plots on the top layer and $\kappa_Z = 1.0$ for the plots in the bottom layer.

A comparison of Table 7 and 8 shows that the BDT analysis perform better than the cut based analysis presented in previous section as expected. One obtains almost factor 2 enhancement in the estimation of the significances for the various BP's considered in our analysis. This is due to the fact that BDT comes with better efficiency for the signal events even though the background efficiency remains almost the same. We have obtained more than 9σ (5σ) significance using BDT (cut based) analysis for all our chosen benchmark points. We further note that the corresponding background contributions have limited sensitivity to the EFT operators introduced here, hence we do not include them in our analysis.

A χ^2 analysis is performed in the two dimensional parameter space of the EFT operator coefficients as well as in coupling modifiers. All the plots show a bounded region which is not entirely closed. This is because the analysis is primarily done in a single channel. Based on the plots in Figure 9 and Figure: 10, it is evident that the inclusion of EFT contributions significantly alter the bounds on the $\kappa_Z - \kappa_B$ plane. It is observed that even with the tight constraints on the operators, presence of CP even operator $\mathcal{O}_{Hq}^{(3)}$ results in visible changes on the bounds in $\kappa_Z - \kappa_B$ plane. The individual impact of the CP odd operator \mathcal{O}_{uW} is relatively small and do not show any significant deviation from the SM predictions. This is mainly because, they do not interfere with SM and the contributions are obtained only at $1/\Lambda^4$ order. However, if we choose a smaller NP scale, for example, $\Lambda = 500$ GeV, which still remains okay with the effective theory limit as seen from the Fig. 6 after taking care of the already existing constraints, the effect from CP odd contributions

enhance roughly by a factor of 16 and has a larger contribution. Similar arguments hold for dimension eight operators, whose inclusion will not affect the conclusions significantly at least with a large NP scale. However, the contributions from $\mathcal{O}_{Hq}^{(3)}$ will still dominate. Therefore, for detecting CP violating NP, dedicated observables are required.

Acknowledgments

SB would like to acknowledge the grant CRG/2019/004078 from DST-SERB, Govt. of India.

A Details of BDT analysis parameters

Feature selection is an integral and significant part of any machine learning analysis. Presence of too many redundant features causes a model to learn unnecessary characteristics, as such we expect the features to have little dependence on one another. The correlation matrix captures the interdependence among the features very accurately. For our BDT model, the feature correlation heatmap is plotted in Figure 11. Darker patches refer to high correlation. Apart from features like p_T^l and p_T^ll , p_T^b and p_T^{bb} , where correlation is expected, most of the features show little to no correlation, enhancing the model’s learnability against general data. Apart from feature selection, another important aspect of model tuning is the hyperparameter optimization. Proper tuning prevents the model from overfitting, resulting in better performance on new data. The optimized hyperparameters for the model are detailed in Table 9.

Hyperparameters for the XGBClassifier model	Optimal value
Number of boosting rounds (<code>n_estimators</code>)	50
Maximum depth of a tree (<code>max_depth</code>)	5
Learning rate for the model (<code>learning_rate</code>)	0.15
Fraction of samples used each tree (<code>subsample</code>)	0.8
Fraction of features used for each tree (<code>colsample_bytree</code>)	1.0
Minimum sum of instance weight in a child (<code>min_child_weight</code>)	50
Minimum loss reduction for further partition (<code>gamma</code>)	0.75
L1 regularization term on weights (<code>reg_alpha</code>)	8
L2 regularization term on weights (<code>reg_lambda</code>)	60
Maximum step size for each iteration (<code>max_delta_step</code>)	2

Table 9: The optimal hyperparameter values for the model mined using GridSearchCV. The objective hyperparameter is fixed at "binary:logistic".

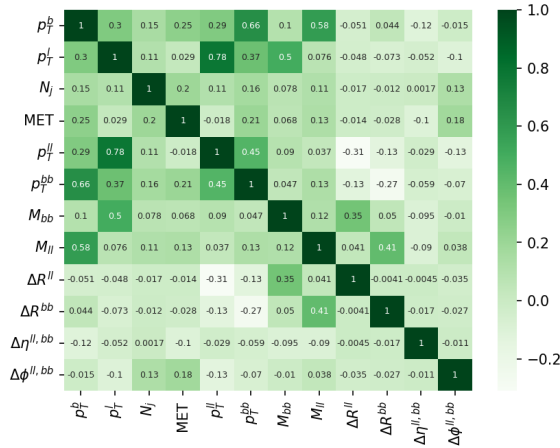


Figure 11: Correlation matrix for the features used in training the XGBoost model.

p_T^l (GeV)	Signal (S)	Background (B)
0 - 25	15	180
25 - 50	244	11933
50 - 75	942	33769
75 - 100	764	37304
100 - 125	732	25895
125 - 150	399	12402
150 - 175	240	6652
175 - 200	167	4323
200 - 225	120	1913
225 - 250	46	863
> 250	153	1810

Table 10: Transverse momentum of the leading lepton for signal and background processes in different bins for a threshold selection of 0.95.

References

- [1] H.E. Logan, *TASI 2013 lectures on Higgs physics within and beyond the Standard Model*, [1406.1786](#).
- [2] PARTICLE DATA GROUP collaboration, *Review of Particle Physics*, [PTEP 2022 \(2022\) 083C01](#).
- [3] B. Grzadkowski, M. Iskrzynski, M. Misiak and J. Rosiek, *Dimension-Six Terms in the Standard Model Lagrangian*, [JHEP 10 \(2010\) 085 \[1008.4884\]](#).
- [4] ATLAS collaboration, *A detailed map of Higgs boson interactions by the ATLAS experiment ten years after the discovery*, [Nature 607 \(2022\) 52 \[2207.00092\]](#).
- [5] CMS collaboration, *A portrait of the Higgs boson by the CMS experiment ten years after the discovery.*, [Nature 607 \(2022\) 60 \[2207.00043\]](#).
- [6] CMS collaboration, *Constraints on anomalous HVV couplings from the production of Higgs bosons decaying to τ lepton pairs*, [Phys. Rev. D 100 \(2019\) 112002 \[1903.06973\]](#).

- [7] I. Anderson et al., *Constraining Anomalous HVV Interactions at Proton and Lepton Colliders*, *Phys. Rev. D* **89** (2014) 035007 [[1309.4819](#)].
- [8] P. Sharma and A. Shivaji, *Probing non-standard HVV ($V = W, Z$) couplings in single Higgs production at future electron-proton collider*, *JHEP* **10** (2022) 108 [[2207.03862](#)].
- [9] S. Dutta, K. Hagiwara and Y. Matsumoto, *Measuring the Higgs-Vector boson Couplings at Linear e^+e^- Collider*, *Phys. Rev. D* **78** (2008) 115016 [[0808.0477](#)].
- [10] N. Desai, D.K. Ghosh and B. Mukhopadhyaya, *CP-violating HWW couplings at the Large Hadron Collider*, *Phys. Rev. D* **83** (2011) 113004 [[1104.3327](#)].
- [11] N.D. Christensen, T. Han and Y. Li, *Testing CP Violation in ZZH Interactions at the LHC*, *Phys. Lett. B* **693** (2010) 28 [[1005.5393](#)].
- [12] S. Dwivedi, D.K. Ghosh, B. Mukhopadhyaya and A. Shivaji, *Distinguishing CP-odd couplings of the Higgs boson to weak boson pairs*, *Phys. Rev. D* **93** (2016) 115039 [[1603.06195](#)].
- [13] F.U. Bernlochner, C. Englert, C. Hays, K. Lohwasser, H. Mildner, A. Pilkington et al., *Angles on CP-violation in Higgs boson interactions*, *Phys. Lett. B* **790** (2019) 372 [[1808.06577](#)].
- [14] J. Brehmer, F. Kling, T. Plehn and T.M.P. Tait, *Better Higgs-CP Tests Through Information Geometry*, *Phys. Rev. D* **97** (2018) 095017 [[1712.02350](#)].
- [15] S. Banerjee, T. Mandal, B. Mellado and B. Mukhopadhyaya, *Cornering dimension-6 HVV interactions at high luminosity LHC: the role of event ratios*, *JHEP* **09** (2015) 057 [[1505.00226](#)].
- [16] S. Banerjee, C. Englert, R.S. Gupta and M. Spannowsky, *Probing Electroweak Precision Physics via boosted Higgs-strahlung at the LHC*, *Phys. Rev. D* **98** (2018) 095012 [[1807.01796](#)].
- [17] S. Banerjee, R.S. Gupta, J.Y. Reiness and M. Spannowsky, *Resolving the tensor structure of the Higgs coupling to Z-bosons via Higgs-strahlung*, *Phys. Rev. D* **100** (2019) 115004 [[1905.02728](#)].
- [18] S. Banerjee, R.S. Gupta, J.Y. Reiness, S. Seth and M. Spannowsky, *Towards the ultimate differential SMEFT analysis*, *JHEP* **09** (2020) 170 [[1912.07628](#)].
- [19] S. Banerjee, R.S. Gupta, O. Ochoa-Valeriano, M. Spannowsky and E. Venturini, *A fully differential SMEFT analysis of the golden channel using the method of moments*, *JHEP* **06** (2021) 031 [[2012.11631](#)].
- [20] S. Banerjee, R.S. Gupta, O. Ochoa-Valeriano and M. Spannowsky, *High energy lepton colliders as the ultimate Higgs microscopes*, *JHEP* **02** (2022) 176 [[2109.14634](#)].
- [21] T. Biswas, A. Datta and B. Mukhopadhyaya, *Following the trail of new physics via the vector boson fusion Higgs boson signal at the Large Hadron Collider*, *Phys. Rev. D* **105** (2022) 055028 [[2107.05503](#)].
- [22] J.Y. Araz, S. Banerjee, R.S. Gupta and M. Spannowsky, *Precision SMEFT bounds from the VBF Higgs at high transverse momentum*, *JHEP* **04** (2021) 125 [[2011.03555](#)].
- [23] I. Brivio and M. Trott, *The Standard Model as an Effective Field Theory*, *Phys. Rept.* **793** (2019) 1 [[1706.08945](#)].
- [24] R. Alonso, E.E. Jenkins and A.V. Manohar, *A Geometric Formulation of Higgs Effective*

- Field Theory: Measuring the Curvature of Scalar Field Space*, *Phys. Lett. B* **754** (2016) 335 [[1511.00724](#)].
- [25] A. Crivellin, M. Ghezzi and M. Procura, *Effective Field Theory with Two Higgs Doublets*, *JHEP* **09** (2016) 160 [[1608.00975](#)].
- [26] Anisha, S. Das Bakshi, J. Chakraborty and S. Prakash, *Hilbert Series and Plethystics: Paving the path towards 2HDM- and MLRSM-EFT*, *JHEP* **09** (2019) 035 [[1905.11047](#)].
- [27] F. del Aguila, S. Bar-Shalom, A. Soni and J. Wudka, *Heavy Majorana Neutrinos in the Effective Lagrangian Description: Application to Hadron Colliders*, *Phys. Lett. B* **670** (2009) 399 [[0806.0876](#)].
- [28] A. Aparici, K. Kim, A. Santamaria and J. Wudka, *Right-handed neutrino magnetic moments*, *Phys. Rev. D* **80** (2009) 013010 [[0904.3244](#)].
- [29] S. Bhattacharya and J. Wudka, *Dimension-seven operators in the standard model with right handed neutrinos*, *Phys. Rev. D* **94** (2016) 055022 [[1505.05264](#)].
- [30] H.-L. Li, Z. Ren, J. Shu, M.-L. Xiao, J.-H. Yu and Y.-H. Zheng, *Complete set of dimension-eight operators in the standard model effective field theory*, *Phys. Rev. D* **104** (2021) 015026 [[2005.00008](#)].
- [31] C.W. Murphy, *Dimension-8 operators in the Standard Model Effective Field Theory*, *JHEP* **10** (2020) 174 [[2005.00059](#)].
- [32] S. Bhattacharya and J. Wudka, *Effective theories with dark matter applications*, *Int. J. Mod. Phys. D* **30** (2021) 2130004 [[2104.01788](#)].
- [33] A. Alloul, N.D. Christensen, C. Degrande, C. Duhr and B. Fuks, *FeynRules 2.0 - A complete toolbox for tree-level phenomenology*, *Comput. Phys. Commun.* **185** (2014) 2250 [[1310.1921](#)].
- [34] C. Degrande, C. Duhr, B. Fuks, D. Grellscheid, O. Mattelaer and T. Reiter, *UFO - The Universal FeynRules Output*, *Comput. Phys. Commun.* **183** (2012) 1201 [[1108.2040](#)].
- [35] J. Alwall, M. Herquet, F. Maltoni, O. Mattelaer and T. Stelzer, *MadGraph 5 : Going Beyond*, *JHEP* **06** (2011) 128 [[1106.0522](#)].
- [36] CMS collaboration, *Observation of Higgs boson decay to bottom quarks*, *Phys. Rev. Lett.* **121** (2018) 121801 [[1808.08242](#)].
- [37] ATLAS collaboration, *Measurements of WH and ZH production in the $H \rightarrow b\bar{b}$ decay channel in pp collisions at 13 TeV with the ATLAS detector*, *Eur. Phys. J. C* **81** (2021) 178 [[2007.02873](#)].
- [38] SMEFT collaboration, *Combined SMEFT interpretation of Higgs, diboson, and top quark data from the LHC*, *JHEP* **11** (2021) 089 [[2105.00006](#)].
- [39] S. Bißmann, C. Grunwald, G. Hiller and K. Kröninger, *Top and Beauty synergies in SMEFT-fits at present and future colliders*, *JHEP* **06** (2021) 010 [[2012.10456](#)].
- [40] C. Grunwald, G. Hiller, K. Kröninger and L. Nollen, *More synergies from beauty, top, Z and Drell-Yan measurements in SMEFT*, *JHEP* **11** (2023) 110 [[2304.12837](#)].
- [41] M. Thomas Arun, K. Deka and T. Srivastava, *Constraining SMEFT BSM scenarios with EWPO and Δ_{CKM}* , [2301.09273](#).
- [42] ATLAS collaboration, *Measurements of differential cross-sections in four-lepton events in 13 TeV proton-proton collisions with the ATLAS detector*, *JHEP* **07** (2021) 005 [[2103.01918](#)].

- [43] ATLAS collaboration, *Combined measurements of Higgs boson production and decay using up to 139 fb^{-1} of proton-proton collision data at $\sqrt{s} = 13 \text{ TeV}$ collected with the ATLAS experiment*, .
- [44] R. Boughezal, E. Mereghetti and F. Petriello, *Dilepton production in the SMEFT at $O(1/\Lambda^4)$* , *Phys. Rev. D* **104** (2021) 095022 [[2106.05337](#)].
- [45] V. Cirigliano, A. Crivellin, W. Dekens, J. de Vries, M. Hoferichter and E. Mereghetti, *CP Violation in Higgs-Gauge Interactions: From Tabletop Experiments to the LHC*, *Phys. Rev. Lett.* **123** (2019) 051801 [[1903.03625](#)].
- [46] R.D. Ball et al., *Parton distributions with LHC data*, *Nucl. Phys. B* **867** (2013) 244 [[1207.1303](#)].
- [47] T. Sjostrand, S. Mrenna and P.Z. Skands, *A Brief Introduction to PYTHIA 8.1*, *Comput. Phys. Commun.* **178** (2008) 852 [[0710.3820](#)].
- [48] M. Cacciari, G.P. Salam and G. Soyez, *FastJet User Manual*, *Eur. Phys. J. C* **72** (2012) 1896 [[1111.6097](#)].
- [49] M. Cacciari, G.P. Salam and G. Soyez, *The anti- k_t jet clustering algorithm*, *JHEP* **04** (2008) 063 [[0802.1189](#)].
- [50] E. Conte, B. Fuks and G. Serret, *MadAnalysis 5, A User-Friendly Framework for Collider Phenomenology*, *Comput. Phys. Commun.* **184** (2013) 222 [[1206.1599](#)].
- [51] F. Cascioli, T. Gehrmann, M. Grazzini, S. Kallweit, P. Maierhöfer, A. von Manteuffel et al., *ZZ production at hadron colliders in NNLO QCD*, *Phys. Lett. B* **735** (2014) 311 [[1405.2219](#)].
- [52] L. Chen, J. Davies, G. Heinrich, S.P. Jones, M. Kerner, G. Mishima et al., *ZH production in gluon fusion at NLO in QCD*, *JHEP* **08** (2022) 056 [[2204.05225](#)].
- [53] J.M. Campbell, J.W. Huston and W.J. Stirling, *Hard Interactions of Quarks and Gluons: A Primer for LHC Physics*, *Rept. Prog. Phys.* **70** (2007) 89 [[hep-ph/0611148](#)].
- [54] M.D. Schwartz, *TASI Lectures on Collider Physics*, in *Proceedings, Theoretical Advanced Study Institute in Elementary Particle Physics : Anticipating the Next Discoveries in Particle Physics (TASI 2016): Boulder, CO, USA, June 6-July 1, 2016*, R. Essig and I. Low, eds., pp. 65–100 (2018), DOI [[1709.04533](#)].
- [55] G. Cowan, K. Cranmer, E. Gross and O. Vitells, *Asymptotic formulae for likelihood-based tests of new physics*, *Eur. Phys. J. C* **71** (2011) 1554 [[1007.1727](#)].
- [56] Y. Coadou, *Boosted decision trees*, [2206.09645](#).
- [57] A.S. Cornell, W. Doorsamy, B. Fuks, G. Harmsen and L. Mason, *Boosted decision trees in the era of new physics: a smuon analysis case study*, *JHEP* **04** (2022) 015 [[2109.11815](#)].
- [58] T. Chen and C. Guestrin, *Xgboost: A scalable tree boosting system*, in *Proceedings of the 22nd ACM SIGKDD International Conference on Knowledge Discovery and Data Mining, KDD '16*, ACM, Aug., 2016, DOI.
- [59] F. Pedregosa, G. Varoquaux, A. Gramfort, V. Michel, B. Thirion, O. Grisel et al., *Scikit-learn: Machine learning in Python*, *Journal of Machine Learning Research* **12** (2011) 2825.
- [60] S. Lundberg and S.-I. Lee, *A unified approach to interpreting model predictions*, 2017.